# Ultrasensitive Chemical Detection Using a Nanocoax Sensor

Huaizhou Zhao,[†,‡] Binod Rizal,[†] Gregory McMahon,[†] Hengzhi Wang,[†] Pashupati Dhakal,[†] Timothy Kirkpatrick,[†] Zhifeng Ren,[†] Thomas C. Chiles,[‡] Michael J. Naughton,[†,*] and Dong Cai[‡,*]

[†]Department of Physics and [‡]Department of Biology, Boston College, Chestnut Hill, Massachusetts 02467, United States

Nanoscale materials and architectures can offer unique and highly sensitive sensors for the detection and identification of target chemical and biological agents for use in environmental monitoring, threat detection, and clinical diagnostics. Schemes involving nanopores, nanowires, microcantilevers, and microcavities have reportedly achieved highly sensitive molecular detection.[1−5] For example, gated single-walled carbon nanotubes (CNTs) have been used to detect $NO_2$ and $NH_3$ gases to parts per million (ppm) levels in Ar,[6] while resistivity changes have been observed in graphene microcrystals upon exposure to those same gases,[7] with a projected limit of detection (LOD) of ∼1 parts per billion (ppb). Metal-oxide-based devices also represent a large category of sensors that have shown high sensitivity to chemicals,[8] such as a Pt-doped $SnO_2$ semiconductor metal oxide sensor with a reported capability of ethanol detection down to parts per billion levels.[9] Other examples include a 3D porous multiwalled CNT/Nafion surface acoustic wave resonator for relative humidity (RH) detection, with a sensitivity of 0.5% RH,[10] and an array of nanomechanical resonators with demonstrated ppb level sensitivity to the detection of the chemical warfare agent simulant diisomethylphosphonate.[11]

While these and related sensing schemes can be all-electronic (i.e., not requiring optical readout), they all require sophisticated nanolithographic techniques to isolate, identify, and integrate electrical contact to the active nanosensor. In general, these are 2D structures, with individual sensing units lying on a planar substrate, which can severely limit access of target molecules to the sensing element. Moreover, fabricating numbers of such individual sensors, useful for increasing molecular detection probabilistics and facilitating multiplexed detection, is a serial and therefore time-consuming

**ABSTRACT**
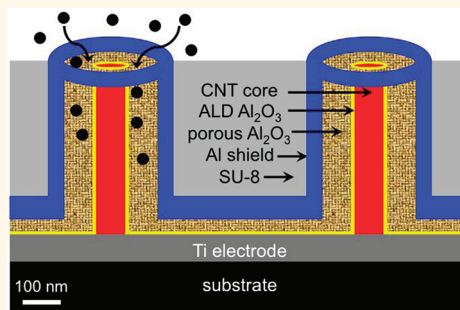


We report on the design, fabrication, and performance of a nanoporous, coaxial array capacitive detector for highly sensitive chemical detection. Composed of an array of vertically aligned nanoscale coaxial electrodes constructed with porous dielectric coax annuli around carbon nanotube cores, this sensor is shown to achieve parts per billion level detection sensitivity, at room temperature, to a broad class of organic molecules. The nanoscale, 3D architecture and microscale array pitch of the sensor enable rapid access of target molecules and chip-based multiplexing capabilities, respectively.

**KEYWORDS:** chemical sensor · nanocoax · nanotube array

chore. Finally, temperatures of several hundred degrees centigrade and detection times of minutes are usually required to achieve the reported sensitivities.

## RESULTS AND DISCUSSION

Here, we present a nanoscale 3D architecture that can afford highly sensitive, room temperature, rapid response, and all-electronic chemical detection. The device is derived from a recently elaborated "nanocoax" array architecture that has so far been employed in novel nanophotonic[12,13] and photovoltaic[14,15] applications. The structure of the nanocoax is shown in the Abstract and in Figure 1. It consists of an array of vertically oriented carbon nanotubes, each conformally coated with a dielectric and a metal to form a coaxial electrode (see Methods and Supporting Information Figure S1). Using only microlithographic techniques,[9,11]
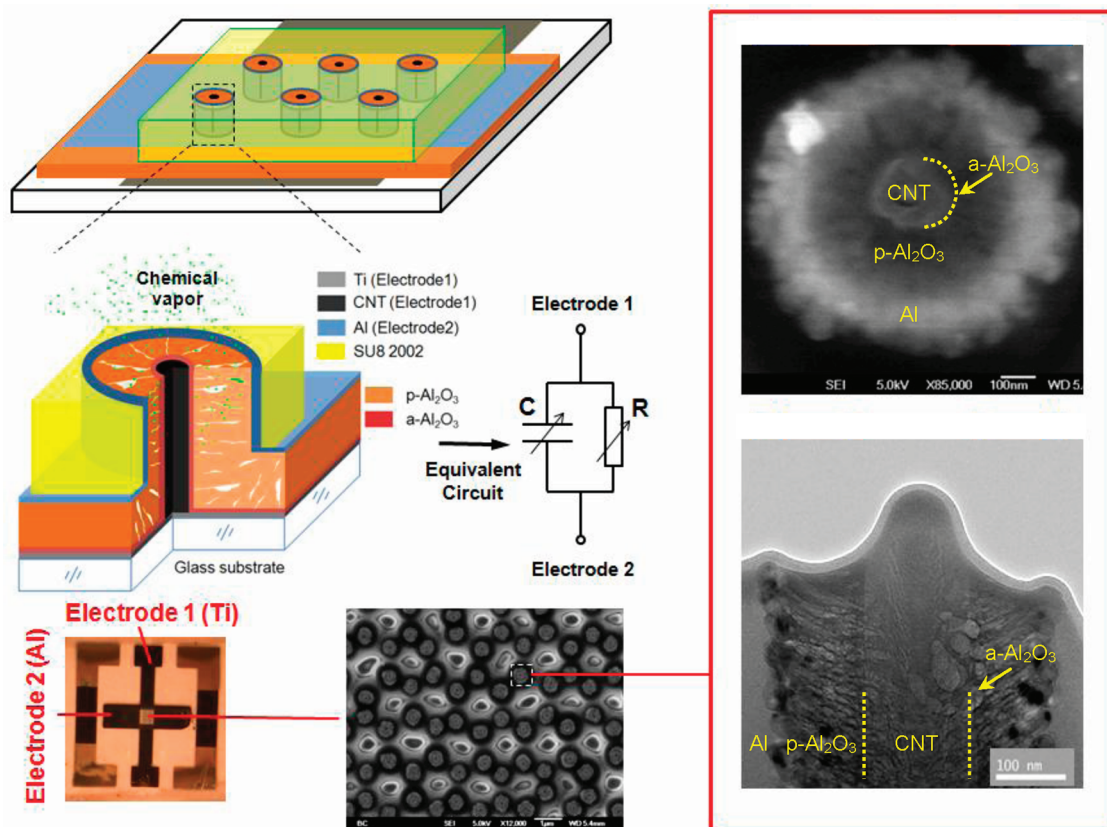
**Figure 1. Nanocoaxial array-based chemical detection platform.** The structure is composed of a CNT, alumina coatings by nonporous atomic layer (a-Al$_2$O$_3$) and porous sputter (p-Al$_2$O$_3$) depositions, and aluminum (Al) coating by sputtering. The array is supported by SU8 polymer. The coaxial units are mechanically polished to open access to the p-Al$_2$O$_3$ for target molecules. The outer (Al) and inner (CNT) coax conductors form nanocoaxial cables whose equivalent circuit is a resistor (R) and capacitor (C) connected in parallel. Each CNT is connected to a bottom titanium (Ti) film forming "Electrode 1"; the outer Al coating forms "Electrode 2". A top view scanning electron microscope (SEM) image at low magnification shows a periodic array of identical nanocoax units. At right are SEM (top) and TEM (bottom) images at higher magnifications, where the multiple components of a unit can be clearly observed. In contrast to a-Al$_2$O$_3$, p-Al$_2$O$_3$ can capture chemical molecules by chemiphysical adsorption, leading to changes in the sensor impedance as well as its components, R and C.

arrays with extremely high spatial density can be prepared, including in multiplexed configurations, with typical 1.5 $\mu$m spacing yielding an areal density of ~$10^8$ units/cm$^2$. Considering that each unit in an array is in fact a coaxial capacitor, target molecules entering porous annuli of such open-ended nanocoaxial wires (*e.g.*, via diffusion and chemical and/or physical adsorption) will cause changes in the dielectric response (capacitance and conductance) in proportion to their number and their static and dynamic dielectric properties. Frequency-dependent dielectric spectroscopy can potentially be employed to identify molecules with some specificity, relying on distinguishable characteristic features in frequency space for specific molecules.[16] We also discuss an experimental measurement process in which the device sensitivity is found to significantly improve under static, as opposed to flowing, conditions.

Initial confirmation of the dielectric detection principle was conveyed by an impedance spectroscopic measurement of sensor capacitance. First, the porosity of sputtered, porous Al$_2$O$_3$ was determined

electrochemically to be ~10% (Methods and Supporting Information Figure S2). Then, dielectric constants of porous Al$_2$O$_3$ infused with air ($\varepsilon_{AO}^A$) and water ($\varepsilon_{AO}^W$) were derived. The calculated *versus* measured sensor capacitance values were 1.4 *versus* 1.1 nF and 2.1 *versus* 2.3 nF, before and after total water infusion, respectively (Methods). Previous reports of humidity sensing based on anodic Al$_2$O$_3$ concern conductivity changes in the presence of water due to acid residues.[17] Sputtered Al$_2$O$_3$, however, has no anionic groups, so our sensor response is dominated by capacitance. Further confirmation was performed by utilizing the sensor for humidity detection. Relative humidity was varied by diluting saturated water vapor in N$_2$ and measuring under dynamic flow (Methods). Data for changes in capacitance $\delta(\Delta C)$ (*i.e.*, after subtracting the N$_2$-only capacitance response) *versus* time for a range of RH values are shown in Figure 2 (inset), due to introduction of vapor + N$_2$ flow to a chamber initiated with pure N$_2$ flow, in such a manner as to maintain constant total flow of 5000 sccm and pressure of $10^5$ Pa (~1 bar).
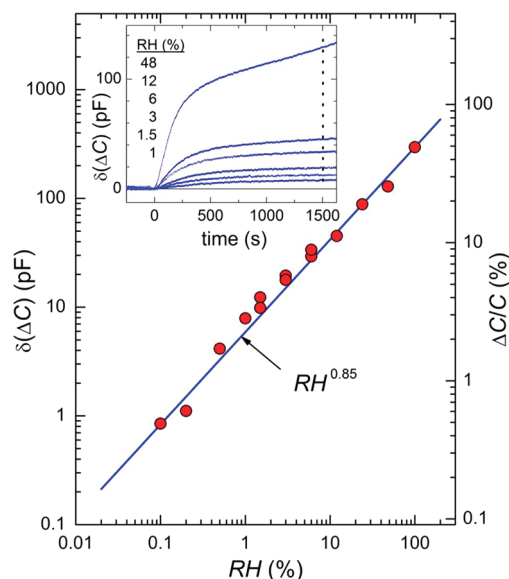
**Figure 2. Humidity detection by the nanocoaxial sensor array.** Capacitance response *vs* time for various levels of relative humidity (inset) and $\delta(\Delta C)$ at 1500 s *vs* RH, showing power-law response across 3 decades in RH. The right scale indicates the corresponding fractional changes in capacitance.

At low humidity (RH $\sim$ 0.1–10%), the temporal response is that of a typical charging capacitor, while at high humidity (RH $\sim$ 30%), an additional dynamic emerges, with a quasi-linear increase in capacitance after an initial saturating phase. Due to this dynamical component, no steady state was indicated within the 1 h observation window. It is possible that, at high RH, volume condensation dominates over surface adsorption in the porous $Al_2O_3$ structure. The gradual wetting of the $Al_2O_3$ toward the bottom of nanocoax could lead to the linear increase that is superimposed on the first exponential component. Accordingly, all sensor responses are compared at a relatively early stage when the dynamics are still single exponential. We have selected $\delta(\Delta C)$ values at 1500 s, as shown by the dotted line in the inset of Figure 2, to characterize the response, summarized in the main panel. A power-law dependence over 3 decades of RH emerges, $\delta(\Delta C) \sim RH^{\beta}$, with $\beta \sim 0.85$ (similar results are obtained for different time selections above $\sim$300 s). This chart can be considered to represent a concentration-dependent response associated with an adsorption isotherm. Note the uniform response across a large dynamic range in concentration. The sensitivity in terms of fractional change in capacitance per RH is $(\delta(\Delta C)/C)/RH \sim 4$ (in %/%) at low RH. The lowest RH tested was 0.1%, equivalent to 16 ppm (V) at 20 °C, more than 3 times lower than a recently reported LOD for porous $Al_2O_3$-based humidity sensors.[18] With moderate improvements in signal-to-noise ratio, we anticipate that such measurements can be extended to the 0.01% RH range or below by using the conventional process.

In order to demonstrate the breadth of utility and high sensitivity of the coaxial array sensor, the device
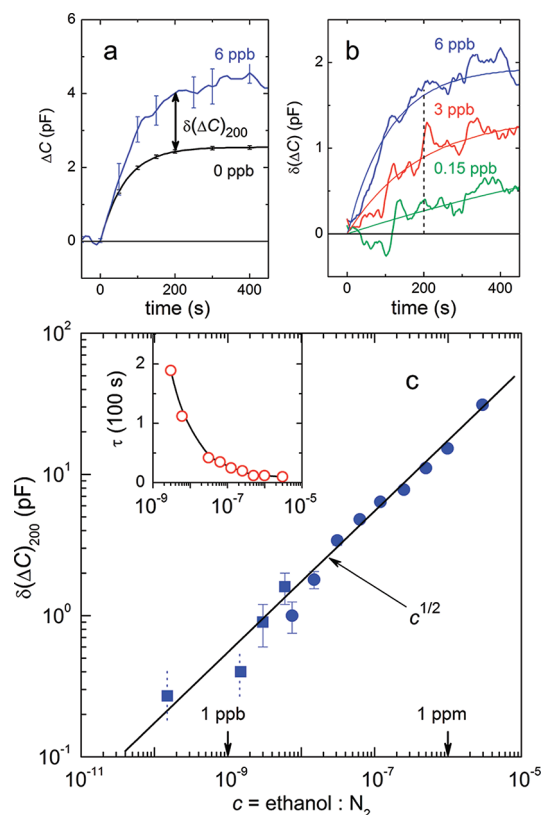


**Figure 3. Nanocoaxial sensor array as high-performance ethanol sensor.** (a) Average responses of ethanol at 6 ppb ($n = 3$) and $N_2$ control (0 ppb, $n = 11$), along with standard deviations, plotted *versus* time, after introduction into an evacuated chamber. (b) Individual ethanol response after subtraction of $N_2$ background, $\delta(\Delta C)$ for concentrations $c =$ 0.15, 3, and 6 ppb, shown overlaid by fits for a charging capacitor (smooth lines). (c) Summary of ethanol response $\delta(\Delta C)_{200}$ (*i.e.*, averages and standard deviations from three responses, each recorded 200 s after ethanol application, as defined in (a)), showing power-law behavior over almost 5 decades in concentration, extending to sub-ppb level. High (circles) and low (squares) concentration regimes were investigated on separate days. Inset: Time constant of sensor response derived from fitting shown in (b). All data were recorded by capacitance bridge and lock-in amplifier at 10 Hz.

was used to detect volatile organic compounds (VOCs) diluted in $N_2$ gas. The measurement process is described in Methods. High-purity nitrogen was used as a control, flowed into the evacuated chamber at 5000 sccm, with a capacitance response of $\sim$0.0025 nF. This is not too far from a calculated change of $\sim$0.001 nF, based on the device geometry and the dielectric constant of 100% pure $N_2$. The capacitance response was recorded under dynamic and static conditions (*i.e.*, without active flow), with the latter providing significantly larger response (Supporting Information Figure S8). The response to the VOC ethanol at various concentrations is shown in Figure 3. In Figure 3a, we show the response to $N_2$ only (depicted as 0 ppb) and ethanol at 6 ppb concentration. The $N_2$ curve represents an average of 11 traces, with error bars indicating the standard deviation. The 6 ppb data are from an average of three sets of data. The net ethanol response

$\delta(\Delta C)$ is plotted in Figure 3b for three representative concentrations (again, each an average of three curves). In general, the temporal response is that of a charging capacitor, $\delta(\Delta C)(t) = \delta(\Delta C)_\infty (1 - e^{-t/\tau})$ (solid lines in Figure 3b), where $\delta(\Delta C)_\infty$ is the steady state amplitude (i.e., as $t \rightarrow \infty$), and $\tau$ is a time constant. One can characterize the response by this $\delta(\Delta C)_\infty$, or by $\delta(\Delta C)_t$ at a particular time $t$. In order to ensure consistency for all concentrations, we have chosen the $t = 200$ s response, indicated as $\delta(\Delta C)_{200}$ in Figure 3. Complete data for ethanol are shown in Figure 3c, plotting this $\delta(\Delta C)_{200}$ versus concentration $c$ on logarithmic scales. Similar to the RH data, a power-law response to $c$ is seen, with $\delta(\Delta C) \sim c^\alpha$ and $\alpha = 0.50 \pm 0.02$, now extending across 5 orders of magnitude, nearly to the 100 parts per trillion (ppt) level. This exponent $\alpha$ is close to that expected from isotherm equations used in phenomenological models by Langmuir (dissociative adsorption) and Freundlich to characterize adsorption in porous media,[19] both varying as $c^{1/2}$, as plotted in the figure. At the lowest concentration, we calculate that each nanocoax unit detects a signal produced by only $\sim$30 ethanol molecules (Methods).

The standard deviations of the $N_2$ control and 6 ppb signals are 0.05 and 0.4 pF, respectively. Considering a $3\sigma$ criterion, we claim a LOD for ethanol of 10 ppb. This represents a proof-of-concept for highly sensitive, nanocoax-based chemical detection. Certain aspects of the device, such as the porosity of the dielectric medium, sensor pretreatment to reduce surface contamination and improve reactivity, and details of the capacitance measurement electronics have not yet been optimized to maximize signal-to-noise ratio and device consistency, as well as add molecular selectivity that would maximally exploit the technical potential of the nanocoax sensor and the new process. The sub-ppb detection potential suggested by Figure 3 is therefore a viable objective for this device. In addition, the 10 ppb LOD shown here surpasses that reported for any $Al_2O_3$-based chemical sensor and for any ethanol chemical sensor.[8,20,21]

With regard to the response time of the device, we show in the inset of Figure 3c the dependence of the time constant $\tau$, obtained from fits of the charging capacitor equation above to the data, as indicated by the smooth lines in Figure 3b. The response is quite rapid (seconds) for concentrations above $\sim$100 ppb and increases to only $\sim$100 s at 6 ppb. Compared to the 10 min response time scale for 20 ppb ethanol detection in one reported case,[17] which we take to represent the state-of-the-art, the present nanocoax-based sensor shows improvement with respect to both LOD and response rate. Considering that employing elevated temperature is a typical strategy for improving chemical sensor performance (e.g., 320 °C in ref 17), we note that the working temperature in the present report is 20 °C. Further improvement with the porous nanocoax may thus be possible at elevated temperatures, which should contribute to higher

Knudsen and Fickian diffusivities that lead to both faster response time and larger response magnitude. This would also improve chemical desorption from the sensor surface, so as to provide rapid recovery in VOC detection (Methods and Supporting Information Figure S7). In our detection cases, due to the differences of absorption efficiency of chemical targets on the porous $Al_2O_3$ between the static and conventional flowing gas processes, the rising and recovery phases show notable differences. For conventional RH detection, $N_2$ flushing is able to recover the sensor on a time scale commensurate with the response to exposure (Supporting Information Figure S7a). However, this observation is only applicable at low RH. When RH is more than $\sim$40%, a longer recovery time to $N_2$ flushing was observed. For ethanol and other VOCs, because of the more efficient absorption by avoiding the as yet ill-defined nontrivial dependence on flow rate, adsorption is not trivially reversible by $N_2$ flushing, so that the sensor can be saturated by low concentrations. In order to effectively recover the sensor and obtain consistent responses to various concentrations, we employed evacuation to initiate the sensor as stated in the Methods. All measurements have subtracted background capacitance that may correspond to pressure jumping between 1 Pa and 1 bar due to purging of $N_2$ gas. This initiation is employed following each application of ethanol (as shown in Supporting Information Figure 7Sb). Further improvements to experimental conditions, such as use of elevated temperatures, can potentially reduce or eliminate the need for pumping in order to achieve rapid and continuous utilization of the sensor.

Porous materials such as $Al_2O_3$ and $SiO_2$ have been widely used in sensor applications, and the porosity of the dielectric in our structure is crucial to the sensor performance. Physical or chemical adsorption/absorption of target molecules onto the surface of the porous medium is believed to be the basis of the molecular capture mechanism. The sorption behavior depends not only on the fluid-wall attraction but also on interactions between the fluid molecules. The corresponding involvement of adsorbate condensation determined by the Kelvin equation largely increases the filled chemical amount compared to that captured in the form of monolayers by other types of materials. Sensitivity at low concentration can therefore be reasonably predicted and demonstrated in our experiments. Additionally, the pore structure makes an interconnected network that facilitates the diffusion of chemical molecules, as well as the sensor response speed shown in the results with VOC detection. We have also experimentally verified the key role of the $Al_2O_3$ porous annulus in our sensor architecture by fabricating a "cavity" coax structure, wherein the $Al_2O_3$ in the coax annulus is preferentially etched in order to form a cavity or hollow coax annulus. The response in this configuration was significantly degraded for all applied
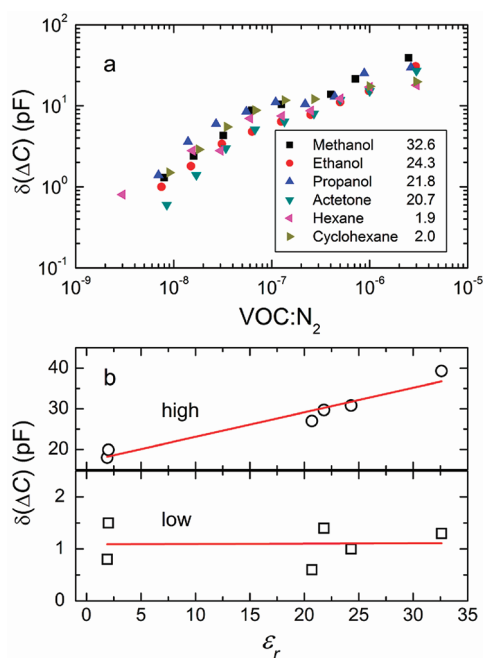
**Figure 4. VOC detection by the nanocoaxial sensor array.** (a) Concentration-dependent responses of various VOC species. Numbers in the figure legends are the values of $\varepsilon_r$ of the chemicals. (b) Relationship between sensor response to VOC and $\varepsilon_r$. The sensor responses at 8 ppb ($\Delta C_{low}$) and 3 ppm ($\Delta C_{high}$) are plotted *vs* respective $\varepsilon_r$ values. Red lines are linear fits.

chemicals, which we ascribe to the far smaller surface area in the cavity compared to that in the $Al_2O_3$ porous annulus coax structure. For example, for 3 ppm ethanol, the sensitivity of a partially etched coax is 10 times lower than that of the porous coax. This result strongly supports the key role of the porous dielectric in the coax sensor.

In addition to ethanol, the sensor was used to detect a variety of other VOCs, including methanol, propanol, acetone, hexane, and cyclohexane, with similar results for concentrations in the parts per billion and parts per million ranges (Figure 4a). It is noteworthy that, at higher concentrations, the response was nominally linear with respect to relative dielectric constant $\varepsilon_r$, while at low concentration, such a correlation was absent (Figure 4b). The mechanism underlying signal transduction of this nanocoaxial capacitor at extremely low chemical concentrations, while highly sensitive, is yet to be clarified. One possibility is that, when the molecule is polar, condensation readily occurs in the $Al_2O_3$ pores, such that at high concentration molecules with high dipole moment (*i.e.*, high $\varepsilon_r$) tend to form multiple layers, with weakly bound outer layers that are thus free to respond to the oscillating electric field. At low concentrations, monolayer formation of absorbed molecules inhibits

such free dielectric response. This could play a role in the weak $\varepsilon$ dependence at low concentration and will be the topic of future investigations.

## CONCLUSION

We report an all-electronic, ambient temperature, rapid-response, and highly sensitive chemical sensor that combines a nanocoaxial array structure containing a nanoporous annulus with a static flow chemical detection scheme. While the cores of the nanocoaxes in the sensor array introduced here are CNTs, essentially any array of highly conducting nanowires will serve the same purpose. In addition to its unique nanostructure, the high sensitivity of our coax-based sensor is strongly related to the static detection method employed. The condensation or adsorption of chemicals on the surface of the pore in the porous annulus appears to be enhanced through this process. We posit increased capillary action as one of the more probable reasons, though further study on the mechanism is required. The device's unique 3D structure affords enhanced access of target molecules to the active sensing element (the porous coax annulus) in comparison to conventional 2D planar structures, and importantly, the dense array yields a multiplicative effect on the signal amplitude. The LOD of sensor is ~10 ppb, although significant potential for improvement to the sub-ppb range is identified. By using the elaborated static measurement and coaxial sensors, we can envision similar ultrasensitive detection levels for small molecules that surpass the present parts per million scale state-of-the-art.[22] Also, this device is amenable to dielectric impedance spectroscopy, by varying the device drive frequency, potentially facilitating "fingerprint" identification of molecules entering the gap, to multiplexing, by forming several independent sections of arrays on a single sensor chip, and to "electronic nose" applications, *via* spatial chemical pattern recognition.[23] This work complements other successful sensing approaches, such as those that employ MEMS or CMOS technologies.[24,25] Considering the potential of the sensor demonstrated thus far using $Al_2O_3$ and other porous media, we can anticipate the achievement of portability, fast recovery time, and high selectivity, using advanced sensor materials and the employed chemical injection method, for the development of an ultrasensitive nanocoax-based chemical detector for additional uses, such as environmental monitoring or noninvasive clinical detection.[26−30]

## METHODS

**Fabrication of Nanocoax Arrays.** Array fabrication begins with CNT growth *via* plasma-enhanced chemical vapor deposition[31]

on polystyrene sphere-patterned substrates,[9,32] followed by successive $Al_2O_3$ dielectric and Al metal depositions *via* sputtering. As shown in the Abstract and Supporting Information

Figure S1, an initial coating outside of the CNTs of 10 nm thick nonporous $Al_2O_3$ was deposited by atomic layer deposition (ALD) to prevent potential shortages between the inner and outer coax electrodes; deposition was carried out at 200 °C in 100 cycles. Following ALD, reactive sputtering was employed to apply ~90 nm thick $Al_2O_3$ by introducing $O_2$ with a 1:4 ratio to argon during Al sputter deposition, at ~0.04 nm/s, with thickness determined by a Sigma SQM-160 monitor on a portion of the substrate not containing CNTs. Each resulting nanocoax is typically ~2 $\mu$m tall, with ~150 nm diameter CNT, 100 nm $Al_2O_3$, and 250 nm thick Al. The CNT and Al correspond to Electrodes 1 and 2, respectively, in Figure 1, overlapping at a $1.0 \times 1.0$ mm$^2$ window that contained the coax array. In order to stabilize the chip structure and electrical properties, an annealing was performed for 8 h between 150 and 200 °C in a vacuum oven. The DC resistance between Electrodes 1 and 2 was nominally in the G$\Omega$ range. The coax arrays were then embedded in SU8-2002 photoresist by spin-coating. After being soft baked at 100 °C for 5 min, SU8 was exposed to UV light for 3 min then hard-baked at 150 °C overnight. Finally, the coax array was polished with a vibratory polisher for 4−6 h until approximately 95% of the nanocoax structures were exposed (as visualized *via* SEM). Note that Electrode 2, which is the external conductor of the nanocoax structure, corresponded to the underlying Ti film.

**Electrochemistry To Characterize Electrical Properties and Porosity of $Al_2O_3$ Thin Film.** Electropolymerization of polypyrrole (PPy) was used to characterize the integrity of the sputter-deposited $Al_2O_3$ film and measure its porosity. To demonstrate the difference of $Al_2O_3$ coatings by sputter deposition and ALD, $Al_2O_3$-coated CNT arrays were subject to electropolymerization by connecting the Ti strip as the working electrode in a three-electrode system. A platinum wire served as the counter electrode, and a AgCl-coated Ag foil was used as a reference electrode. The buffer contained 0.5 M pyrrole and 0.1 M NaCl. Cyclic voltammetry was performed with the voltage scanned from 0 to 0.9 V at 100 mV/s for 10 cycles.

In general, the porous structure can generate leakage in the $Al_2O_3$ film. In a liquid environment for PPy electropolymerization, electrolytes and pyrrole monomers can diffuse into the film and support electrochemical reactions at the CNT surface, provided an oxidative voltage is applied. Because PPy is a conductive polymer, polymerization will proceed in the pore structures and continue outside the film after the pores are filled in the sputter-deposited $Al_2O_3$ (Supporting Information Figure S2a,b). In contrast, when the CNT array was coated by ALD $Al_2O_3$, the surface was completely insulated by the compact coating and no PPy deposition was observed (Supporting Information Figure S2c).

To determine the porosity, galvanostatic deposition of PPy was conducted on a Ti-metalized glass with sputtered $Al_2O_3$ film.[33] A constant 5 $\mu$A current was applied to the sample in the same buffer mentioned above. The potential *versus* time was recorded as an indication of different deposition phases by which the amount of PPy filling into the pores was determined (Supporting Information Figure S3). The potential recorded during the galvanostatic deposition indicated multiple phases of the reaction. The total charge of PPy filling the porous cavities during phase B−C in Supporting Information Figure S3 can be converted to volume of PPy, also volume of porous cavities $V_{cav}$ according to $V_{PPy} = V_{cav} = mQ_{PPy}/(F\sigma)$, where $m$ is the molecular weight of pyrrole, $Q_{PPy}$ the total charge from PPy filling into the porous cavities, $F$ the Faradic constant, and $\sigma$ the density of pyrrole, equal to 1 mg/mm$^3$. The porosity percentage $\phi$ can then be calculated by $\phi = V_{cav}/V_{Al_2O_3} \times 100$, where $V_{Al_2O_3}$ is the volume of $Al_2O_3$, calculated based on the thickness of $Al_2O_3$ coating. As derived from Supporting Information Figure S3, $\phi$ was 10% for the sputter-deposited $Al_2O_3$ coating.

**Spectroscopic Measurements with a Gamry Reference600 Potentiostat.** A polypropylene O-ring was attached to the sensor chip center area encircling the nanocoax array in order to contain a test liquid. A two-electrode electrochemical system was configured by using the top Al film (Electrode 1 in Figure 1) as the combined reference and counter electrodes and the Ti film (Electrode 2) as the working electrode. An AC sine-wave voltage (10 mV peak-to-peak) was applied to the coax chip. The maximum frequency range was from 0.01 Hz to 1 MHz with 20 impedance readings per decade. The impedance data were analyzed using Echem

Analysis software (Gamry, Inc.). Note that before loading the sample, the sensor chips were thoroughly dried in a vacuum oven at 90 °C for 1 h.

To confirm the dielectric measurement of the sensor, impedance spectroscopy was conducted to obtain sensor capacitance without and with water infusion. As shown in Supporting Information Figure S4, the corresponding capacitance values were 1.1 and 2.3 nF at 10 Hz. On the basis of the geometry of the nanocoax array, we can calculate a base capacitance (with dry air or water in the porous $Al_2O_3$ annulus). The capacitance contains contributions from both the nanocoax array and the basal areas between coaxes, given by the two terms in the following expression:

$$C_o = C_{coax} + C_{basal} = N\varepsilon_o \varepsilon_{AO}^A [2\pi \mathcal{l}/\ln(r_2/r_1) + A/d]$$

Here, $\varepsilon_o$ is the permittivity of free space, the nanotube radius was $r_1 = 75$ nm, and the alumina thickness was $r_2 - r_1 = 100$ nm, such that the inner radius of the outer conductor was $r_2 = 175$ nm. On the basis of electron microscopic information, the height or length of a nanocoax (after the final polish step) was $\mathcal{l} = 1.5$ $\mu$m. For the basal (second) term above, device area $A = 1.0$ mm$^2$ and the dielectric thickness was $d = 150$ nm, which results from a deposition that yields 100 nm $Al_2O_3$ radial thickness on the CNTs. Given the dielectric constant of nonporous alumina, $\varepsilon_{AO} = 9.3$, and porosity $\phi = 0.1$, the effective dielectric constant of porous alumina $\varepsilon_{AO}^A$ (filled with dry air of dielectric constant $\varepsilon^A \sim 1$) can be calculated using Maxwell Garnett's derivation for spherical inclusions (pores) in a porous matrix,[34] given by

$$\varepsilon_{AO}^A/\varepsilon_{AO} = 1 + 3\varphi \left( \frac{\varepsilon^A - \varepsilon_{AO}}{\varepsilon^A + 2\varepsilon_{AO}} \right) / \left( 1 - \varphi \left( \frac{\varepsilon^A - \varepsilon_{AO}}{\varepsilon^A + 2\varepsilon_{AO}} \right) \right)$$

or by solving Bruggeman's expression,[35] generalized to treat the matrix and inclusion as symmetrically interpenetrating media

$$\varphi \left( \frac{\varepsilon^A - \varepsilon_{AO}^A}{\varepsilon^A + 2\varepsilon_{AO}^A} \right) + (1 - \varphi) \left( \frac{\varepsilon_{AO} - \varepsilon_{AO}^A}{\varepsilon_{AO} + 2\varepsilon_{AO}^A} \right) = 0$$

At low porosity, the resulting $\varepsilon_{AO}^A$ values, 8.12 and 8.16, respectively, are nearly identical. We used their average, $\varepsilon_{AO}^A = 8.14$. Taken together, these yield $C_0 = 1.42$ nF, close to the measured value.

The effective dielectric constant of the alumina film when the porous spaces were filled with water, $\varepsilon_{AO}^W$, is found to be between 10.4 and 11.7, depending whether one employs the Clausius−Mossotti equation

$$\frac{\varepsilon_{AO}^W - 1}{\varepsilon_{AO}^W + 2} = \varphi \frac{\varepsilon^W - 1}{\varepsilon^W + 2} + (1 - \varphi) \frac{\varepsilon_{AO} - 1}{\varepsilon_{AO} + 2}$$

or Bruggeman's expression above, replacing $\varepsilon_{AO}^A$ by $\varepsilon_{AO}^W$, and using $\varepsilon^W = 80$ as the dielectric constant of water. Due to the change of dielectric constant, the capacitance of the chip is calculated to be 1.8−2.1 nF, again close to the 2.3 nF measurement shown in Supporting Information Figure S4.

**Capacitance Measurements with Capacitance Bridge for Humidity and Chemical Detection.** Measurements were conducted in a prototype recording chamber shown in Supporting Information Figure S5. The chamber is air-tight with valves for gas inlet, pumping, and exhaust. A pin socket provided the electrical connections from a lock-in amplifier (LIA) connected to a capacitance bridge to the sensor electrodes and shielding chassis. To measure the capacitance, a Stanford Research model 830 LIA was set as follows: voltage 0.100 V; frequency 10 Hz; time constant 3 s; and sensitivity 10 $\mu$V. This was mated to a General Radio Model 1616 high precision capacitance bridge. A gas dilution system was constructed and used to control the concentrations of humidity and chemical vapors (Supporting Information Figure S6). For humidity measurements, moisture-saturated $N_2$ from a bubbling bottle was diluted by ultrahigh purity $N_2$ according to the ratio of their flow rates. For VOCs, stock gases commercially prepared at ~3 ppm[36] were diluted by ultrahigh purity $N_2$. The concentrations were determined by the flow rate ratio of the chemical gas, and the dilutant $N_2$ gas

was controlled by mass flow controller. The purity and concentration of each gas was manufacture-certified based on gas chromatography. For all measurements, the gases were introduced into the chamber at 5000 sccm total flow rate. The measurement procedures were as follows: (1) Establish all electrical and pneumatic connections, close chamber, and evacuate system until capacitance and pressure stabilize. Here, the vacuum level corresponded to 1 Pa. (2) Balance the capacitance bridge (capacitance and dissipation). (3) Purge and pump the chamber three times with $N_2$. (4) Introduce mixtures of the chemical gas and $N_2$ at different ratios to supply at the designated concentrations. (5) *Dynamic*: Maintain flow and 1 bar pressure during data recording. *Static*: Stop flow and maintain 1 bar pressure during data recording.

**Detection Sensitivity Calculation.** This calculation estimates the minimum number of molecules that can be detected by the nanocoax sensor. The required parameters for the calculations include: $V_{mol}$, the molar volume of an ideal gas at 25 °C, corresponding to 24.465 L/mol; $V_{cham}$, the volume of the measurement chamber, approximately 0.2 L; $S_{cham}$, the internal surface area of the chamber, calculated to be $\sim 2 \times 10^4$ mm²; $N$, the total number of nanocoax units, approximately $1 \times 10^6$; $S_{array}$, the adsorption area of the sensor chip, designed to be 1 mm²; $[EtOH]_{min}$, the minimum ethanol concentration detected, 150 ppt; and $A_0$, Avogadro's constant, $6.023 \times 10^{23}$ molecules/mol. At 1 bar, the number of ethanol molecules $N_{EtOH}$ in the chamber is calculated by $N_{EtOH} = (V_{cham}/V_{mol})A_0[EtOH]_{min}$. Assuming all ethanol molecules were adsorbed to the surfaces, the number of molecules captured by the sensor $N_{chip}$ is $N_{chip} = N_{EtOH}S_{array}/S_{cham}$. The number of ethanol molecules detected by each nanocoax is then $N_{coax} = N_{chip}/N \sim 30$.

**Rising and Recovery Phase in Humidity and Ethanol Detection.** We show the time-dependent sensor response to 3% RH under the dynamic detection process (Supporting Information Figure S7a), as well to a series of ethanol concentrations under the static detection process (Supporting Information Figure S7b). The static detection model shows much more rapid response to the range of concentration introductions than does the dynamic model performed at 3% RH. In terms of the sensor recovery, the dynamic detection model used for 3% RH was operated under constant $N_2$ flow. We note here that complete recovery was not necessary to ensure good repeatability of response to certain RH levels. For the recovering phase in the static model in ethanol detection, we intentionally initiated the sensor by vacuum pumping to ensure consistent measurements for different concentrations, although we realized that $N_2$ flow might help to reduce the recovering time, and the complete recovery may not be necessary to its followed detections, as it does in RH measurement.

**Comparison of Sensor Responses in the Dynamic and Static Models.** As shown in Supporting Information Figure S8, both static and dynamic processes were investigated for $N_2$ and ethanol detection, with 0.25 and 1.0 ppm shown. For the response to pure nitrogen (top panel), it can be seen that sensor response decreased in a nontrivial manner with increasing gas flow rate. Extensive investigations led us to conclude that the gas flow served in some sense to flush impurities from the array surface, with higher flow flushing more aggressively. Once fully (or at least, largely) flushed at 5000 sccm, the response to pure $N_2$ was minimized to the ~2.5 pF value shown as the open circle. This flushing process was employed prior to the subsequent introduction of every finite VOC concentration. A similar reduction of net dynamic VOC response $\delta(\Delta C)$ with flow rate was observed (bottom panel of Figure S8). The understanding here is that the dynamic process suppresses adsorption of target molecules into the porous dielectric, leading to reduced response with respect to that from static detection model (again, after gas entry at 5000 sccm to reach the desired concentration and zero flow rate after pressure reaches 1 bar within a few seconds). On the contrary, the static model may facilitate adsorption, and thus high response can be obtained. The latter is indicated for both 0.25 and 1.0 ppm by the open symbols. As mentioned in the main text, the nanoporous coax annulus appears to facilitate enhanced capillary action under static flow conditions.

## REFERENCES AND NOTES

1. Fan, F.-R. F.; Bard, A. J. Electrochemical Detection of Single Molecules. *Science* **1995**, *267*, 871–874.
2. Chen, P.; Gu, J.; Brandin, E.; Kim, Y. R.; Wang, Q.; Branton, D. Probing Single DNA Molecule Transport Using Fabricated Nanopores. *Nano Lett.* **2004**, *4*, 2293–2298.
3. Shekhawat, G.; Tark, S.-H.; Dravid, V. P. MOSFET-Embedded Microcantilevers for Measuring Deflection in Biomolecular Sensors. *Science* **2006**, *311*, 1592–1595.
4. Armani, A. M.; Kulkarni, R. P.; Fraser, S. E.; Flagan, R. C.; Vahala, K. J. Label-Free, Single-Molecule Detection with Optical Microcavities. *Science* **2007**, *317*, 783–787.
5. Snow, E. S.; Perkins, F. K.; Houser, E. J.; Badescu, S. C.; Reinecke, T. L. Chemical Detection with a Single-Walled Carbon Nanotube Capacitor. *Science* **2005**, *307*, 1942–1945.
6. Kong, J.; Franklin, N. R.; Zhou, C.; Chapline, M. G.; Peng, S.; Cho, K.; Dai, H. Nanotube Molecular Wires as Chemical Sensors. *Science* **2000**, *287*, 622–625.
7. Schedin, F.; Geim, A. K.; Morozov, S. V.; Hill, E. W.; Blake, P.; Katsnelson, M. I.; Novoselov, K. S. Detection of Individual Gas Molecules Adsorbed on Graphene. *Nat. Mater.* **2007**, *6*, 652–655.
8. Tricoli, A.; Righettoni, M.; Teleki, A. Semiconductor Gas Sensors: Dry Synthesis and Application. *Angew. Chem., Int. Ed.* **2010**, *49*, 7632–7659.
9. Ivanov, P.; Llobet, E.; Vilanova, X.; Brezmes, J.; Hubalek, J.; Correig, X. Development of High Sensitivity Ethanol Gas Sensors Based on Pt-Doped $SnO_2$ Surfaces. *Sens. Actuators, B* **2004**, *99*, 201–206.
10. Sheng, L.; Dajing, C.; Yuquan, C. A Surface Acoustic Wave Humidity Sensor with High Sensitivity Based on Electrospun MWCNT/Nafion Nanofiber Films. *Nanotechnology* **2011**, *22*, 265504–265510.
11. Bargatin, I.; Myers, E. B.; Aldridge, J. S.; Marcoux, C.; Brianceau, P.; Duraffourg, L.; Colinet, E.; Hentz, S.; Andreucci, P.; Roukes, M. L. Large-Scale Integration of Nanoelectromechanical Systems for Gas Sensing Applications. *Nano Lett.* **2012**, DOI: 10. 1021/nl2037479.
12. Rybczynski, J.; Kempa, K.; Herczynski, A.; Wang, Y.; Naughton, M. J.; Ren, Z. F.; Huang, Z. P.; Cai, D.; Giersig, M. Subwavelength Waveguide for Visible Light. *Appl. Phys. Lett.* **2007**, *90*, 021104.
13. Kempa, K.; Wang, X.; Ren, Z. F.; Naughton, M. J. Discretely Guided Electromagnetic Effective Medium. *Appl. Phys. Lett.* **2008**, *92*, 043114.
14. Naughton, M. J.; Kempa, K.; Ren, Z. F.; Gao, Y.; Rybczynski, Y.; Argenti, N.; Gao, W.; Wang, Y.; Peng, Y.; Naughton, J. R.; et al. Efficient Nanocoax-Based Solar Cells. *Phys. Status Solidi RRL* **2010**, *4*, 181–183.
15. Paudel, T.; Rybczynski, J.; Gao, Y.; Lan, Y. C.; Peng, Y.; Kempa, K.; Naughton, M. J.; Ren, Z. F. Nanocoax Solar Cells Based on Aligned Multiwalled Carbon Nanotube Arrays. *Phys. Status Solidi* **2011**, *A208*, 924–927.
16. Kim, J.-M.; Oh, D. H.; Park, J.-H.; Cho, J.-W.; Kwon, Y.; Cheon, C.; Kim, Y.-K. Permittivity Measurements up to 30 GHz Using Micromachined Probe. *J. Micromech. Microeng.* **2005**, *15*, 543–550.
17. Khanna, V. K.; Nahar, R. K. Surface Conduction Mechanisms and the Electrical Properties of $Al_2O_3$ Humidity Sensor. *Appl. Surf. Sci.* **1987**, *28*, 247–264.

18. Dhanekar, S.; Islam, T.; Islam, S. S.; Sengupta, K.; Saha, D. Effect of Organic Vapour on Porous Alumina-Based Moisture Sensor in Dry Gases. *Sens. Trans. J.* **2009**, *6*, 117–127.

19. Corapcioglu, M. Y. *Advances in Porous Media*; Elsevier: Amsterdam, 1996; Vol. 3.

20. Tricoli, A.; Pratsinis, S. E. Dispersed Nanoelectrode Devices. *Nat. Nanotechnol.* **2010**, *5*, 54–60.

21. Kauffman, D. R.; Star, A. Carbon Nanotube Gas and Vapor Sensors. *Angew. Chem., Int. Ed.* **2008**, *47*, 6550–6570.

22. D'Arienzo, M.; Armelao, L.; Mari, C. M.; Polizzi, S.; Ruffo, R.; Scotti, R.; Morazzoni, F. Macroporous $WO_3$ Thin Films Active in $NH_3$ Sensing: Role of the Hosted Cr Isolated Centers and Pt Nanoclusters. *J. Am. Chem. Soc.* **2011**, *133*, 5296–5304.

23. Sysoev, V. V.; Strelcov, E.; Sommer, M.; Bruns, M.; Kiselev, I.; Habicht, W.; Kar, S.; Gregoratti, L.; Kiskinova, M.; Kolmakov, A. Single-Nanobelt Electronic Nose: Engineering and Tests of the Simplest Analytical Element. *ACS Nano* **2010**, *4*, 4487–4494.

24. Hagleitner, C.; Hierlemann, A.; Lange, D.; Kummer, A.; Kerness, N.; Brand, O.; Baltes, H. Smart Single-Chip Gas Sensor Microsystem. *Nature* **2001**, *414*, 293–296.

25. Gardner, J. W.; Pike, A.; de Rooij, N. F.; Koudelka-Hep, M.; Clerc, P. A.; Hierlemann, A.; Göpel, W. Integrated Array Sensor for Detecting Organic Solvents. *Sens. Actuators, B* **1995**, *26*, 135–139.

26. Cao, W. Q.; Duan, Y. Breath Analysis: Potential for Clinical Diagnosis and Exposure Assessment. *Clin. Chem.* **2006**, *52*, 800–811.

27. Righettoni, M.; Tricoli, A.; Pratsinis, S. E. Si:$WO_3$ Sensors for Highly Selective Detection of Acetone for Easy Diagnosis of Diabetes by Breath Analysis. *Anal. Chem.* **2010**, *82*, 3581–3587.

28. Righettoni, M.; Tricoli, A.; Pratsinis, S. E. Thermally Stable, Silica-Doped $\varepsilon$-$WO_3$ for Sensing of Acetone in the Human Breath. *Chem. Mater.* **2010**, *22*, 3152–3157.

29. Sahab, Z. J.; Semaan, S. M.; Sang, Q.-X. Methodology and Applications of Disease Biomarker Identification in Human Serum. *Biomarker Insights* **2007**, *2*, 21–43.

30. Goulart, L. R.; Vieira, C. U.; Fresehi, A. P.; Capparelli, F. E.; Fujimura, P. T.; Almeida, J. F.; Ferreira, L. F.; Goulart, I. M.; Brito-Madurro, A. G.; Madurro, J. M. Biomarkers for Serum Diagnosis of Infectious Diseases and Their Potential Application in Novel Sensor Platforms. *Crit. Rev. Immunol.* **2010**, *30*, 201–222.

31. Ren, Z. F.; Huang, Z. P.; Xu, J. W.; Wang, J. H.; Bush, P.; Siegal, M. P.; Provencio, P. N. Synthesis of Large Arrays of Well-Aligned Carbon Nanotubes on Glass. *Science* **1998**, *282*, 1105–1107.

32. Cai, D.; Ren, L.; Zhao, H.; Xu, C.; Zhang, L.; Yu, Y.; Wang, H.; Lan, Y.; Roberts, M. F.; Chuang, J.; *et al.* A Molecular-Imprint Nanosensor for Ultrasensitive Detection of Proteins. *Nat. Nanotechnol.* **2010**, *5*, 597–601.

33. Harraza, F. A. Electrochemical Polymerization of Pyrrole into Nanostructured p-Type Porous Silicon. *J. Electrochem. Soc.* **2006**, *153*, C349–C356.

34. Garnett, J. C. M. Colours in Metal Glasses and in Metallic Films. *Philos. Trans. R. Soc. London* **1904**, *A 203*, 385–420.

35. Bruggeman, D. A. G. Berechnung Verschiedener Physikalischer Konstanten von Heterogenen Substanzen. *Ann. Phys.* **1935**, *24*, 636–679.See also Bohren, C. F.; Huffman, D. R. *Absorption and Scattering of Light by Small Particles*; Wiley: New York, 1983; p 213.

36. Airgas, Inc. Salem, NH.